Vacuum 141 (2017) 222–229

Contents lists available at ScienceDirect

Vacuum

journal homepage: www.elsevier.com/locate/vacuum

# Influence of erbium substitution on the crystal and electronic properties of $FeBO_3$ oxide

Osman Murat Ozkendir [a, b, *], Abdulcelil Yuzer [b]

[a] Mersin University, Faculty of Technology, Energy Systems Engineering, Tarsus, Turkey
[b] Mersin University, Institute of Natural Science, Dept. of Nanotechnology and Advanced Materials Mersin, Turkey

ARTICLE INFO

*Article history:*
Received 21 March 2017
Received in revised form
11 April 2017
Accepted 12 April 2017
Available online 14 April 2017

*Keywords:*
Magnetic materials
Crystal structure
Oxides
XAFS (EXAFS and XANES)
Electronic structure

ABSTRACT

Influence of rare earth erbium substitution in the $FeBO_3$ material was investigated on its crystal and electronic properties. Studies were mainly carried by the absorption spectroscopy techniques (XAS) in coordination with the x-ray diffraction (XRD) patterns. Crystal structure properties of the samples were studied by x-ray absorption fine structure spectroscopy (XAFS) technique as a complementary probe of $FeBO_3$ material at the room temperatures (RT). During the study, 4*f* level of Er was selected as the main playground due to their interesting relations that may yield fruitful physical phenomena in the materials. Besides, 4*f*-3*d* interplay were determined to emerge dominant interactions causing phase transitions both in crystal and magnetic structures of the samples. With the increasing Erbium substitutions, interesting electronic and magnetic properties were observed in the samples like; varying electrical resistivity of the samples and related crystal phase transition etc.



## 1. Introduction

Transition metals (TM) have an important place in current technological applications due to the possibility of emerging interesting pecularities via the molecular interplays of their partly filled *d* shell. Their abundance in the earths crust and being inexpensive than most other elements, transition metal oxides (TMO) and alloys have become indispensable for most studies [1–8]. Unoccupied *d* shell has five-fold degeneracy and cause different oxidation states that can yield highly desired optical, electronic or magnetic properties for technological applications. The high demand for TMOs in scientific studies is mainly related to the high likelihood of exhibiting electronic properties and desirable magnetic behavior in a chemical environment.

In this study, ferric borate ($FeBO_3$) material was selected as the parent oxide for the investigations. $FeBO_3$ material is a product of $Fe_2O_3$ and $B_2O_3$ binary systems where irons are linked to the oxygen with a tetrahedral coordination, i.e. Fe-$BO_3$. It is an intensively studied member of the transition metal Boron oxides group with $M^{3+}BO3$ general formula and reported with a weak antiferromagnetic ordering above the room temperature ($T_N = 348$ K) [4]. $FeBO_3$ has been reported in the literature as formed in a rhombohedral geometry with a space group of "R3c:H" [6,9]. The study is aimed to probe the influence of a heavy fermion rare earth (RE), Erbium, substitution on the crystal and electronic properties of the $FeBO_3$ oxides according to the general formula $Er_xFe_{1-x}BO_3$. RE element erbium was chosen to observe the influence of the *f*-levels' activity both in the bonding mechanism and on the magnetic properties. 4*f* levels of the rare earth (RE) metals attract huge attentions due to highly active role in electronic interactions. The interplay between 3*d* and 4*f* shells of the TM and RE material is the core of the study. This study will also be a strong candidate to understand the d-f interactions that provide useful background informations for future studies.

There are two end products in this study; $FeBO_3$ and $ErBO_3$. $ErBO_3$ is a member of the rare-earth oxiborate (REO) materials and show reported abilities like nonlinear optical properties [10]. Besides, REO's also attracting much interest in the high temperature superconductor cuprate studies due to showing huge magneto resistance properties. REO's are also known as a powerful member of strongly correlated electron systems (SCES), like $FeBO_3$, among the oxiborate members of TMO's [11]. SCES characteristics of REO's and TMO's, they often participate in the same research topics. Rare-Earth orthoferrite material family is a good example for such a participation and they were reported as revealing interesting phenomena as a result of the electronic and magnetic interactions

* Corresponding author. Mersin University, Faculty of Technology, Energy Systems Engineering, Tarsus, Turkey.
*E-mail address:* ozkendir@gmail.com (O.M. Ozkendir).

http://dx.doi.org/10.1016/j.vacuum.2017.04.021
0042-207X/

[12–14].

Strong electronic correlations between 3*d* and 4*f* levels were subject to many studies in the past and today it still seems a strong candidate who sets the desired characteristics for future studies. The atomic content of the formula $Er_xFe_{1-x}BO_3$ make the samples both a member of REO and TMO materials group and has not been subject to any study, yet. Also, boron in the samples has an import role to limit the substitution due to the higher electron affinity by causing electron deficiency in the bulk with its highly vacant *p*-orbitals. Besides, high thermal stability of borates make them an important tool for high temperature devices and nonlinear optical materials [4].

## 2. Materials and method

The rare-earth oxiborate samples with general formula $Er_xFe_{1-x}BO_3$, where x has value as 0, 0.2, 0.4, 0.6 and 1, were synthesized from the stoichiometric mixtures of $Er_2O_3$, $Fe_2O_3$ and $B_2O_3$ powders as starting materials with high purity (>99.99% Alfa-Aesar) by the solid state reaction method. Powders were mixed and milled in Retsch rm200 with agate ball for 30 min at 100 rpm speed and annealed in air at 550 °C for 4 h. After the annealing process, powders milled again for 30 min and annealed in air at 950 °C for 48 h. Due to high noise in the data of the sample for x = 0.8, it was removed from the analysis and treated as a distorted sample. The reason for the high noise in the data was mainly determined as a result of notable boron deficiency in the sample. Boron atoms have a high tendency to bond with oxygens strongly due to its higher electronegativity. They can form isolated ligands ($B_2O_3$ oxides) and bond to iron and erbium atoms weakly. It is known that boron oxide ligands melt over 500 C heating processes and due to over annealing, isolated boron-oxide complexes melted away during the annealing the process.

To study the crystal properties of the samples, XRD patterns were taken at the Advanced Materials Research Center (MEITAM) laboratories of Mersin University with Rigaku Smartlab model. XRD data were analyzed by the MAUD software which has a name from the words “Material Analysis Using Diffraction” and it is a software for diffraction/reflectivity analysis that mainly based on the Rietveld method. The XRD patterns of the samples were fitted with the phase cards of the known crystal structures taken from the Crystallography Open Database [15].

Electronic properties of the samples were studied with the collected x-ray absorption spectroscopy (XAS) data at MAX-Lab synchrotron radiation facility of Lund University in Lund, Sweden. Fe $L_{3,2}$-edge and O K-edge XAS measurements were performed at Beamline I1011 on MAX-Lab in TEY (Total Electron Yield) mode at room temperature and under ultra-high vacuum (UHV) (~$10^{-10}$ Torr) conditions. The endstation UHV system provides low vacuum in the chamber that enables the scientist to collect high quality data with one preparation chamber equipped with a sputter gun, LEED, and auxiliary ports for user supplied equipment. The chamber is also equipped with an octupole magnet for magnetic data collection by the x-ray magnetic circular/linear dichroism (XMCD/XMLD) techniques.

The beamline is located on the ring MAX-II, using an elliptically polarizing undulator and provides soft x-ray with a variable polarization state [16]. The technique provides rich data collection for investigations on the electronic structure of the interested materials. The XAS region of the absorption spectra lie between an energy range of approximately 30 eV below and 40 eV above the main absorption edge of the elements. From the collected data, one can extract information about the bonding properties, electronic structure of the interested atom with its local atomic arrangements in the materials [17–19].

To perform detailed crystal structure analysis, additional EXAFS (Extended X-ray Absorption Fine Structure) measurements in the hard x-ray region were performed for Er $L_3$ -edge and Fe K-edge of the $Er_xFe_{1-x}BO_3$ samples. The data were collected at Beamline-BL8:XAS of Siam Photon (SLRI) Synchrotron Radiation facility in Nakhon Ratschasima, Thailand [20,21]. The beamline BL8 operates for X-ray Absorption Spectroscopy, serves a high flux light from a bending magnet and has an energy range from 1.25 keV to 10 keV. During the measurements, data were collected at room temperature in transmission mode.

## 3. Results and discussion

Electrical resistivity of the studied samples were measured at the room temperatures (RT) by the four-probe technique and results were around 2.0–14.0 × $10^6$ *ohm cm* which fall in the category of weak semiconductors as given in Fig. 1. According to the results, the samples with lower Er concentrations have close resistance values. However, among the samples, the sample for x = 0.6 has the highest resistivity, while x = 0.4 sample has the lowest value.

The electrical resistivity of the materials are also related to the crystal texture properties of the samples. Several studies reported the relation between grain sizes and the electrical conductivity of polycrystalline materials with the importance of the porosity and larger grain size in materials [22]. Studies revealed that higher porosity and grains support the electronic transportation in the materials to longer distances by providing appropriate media that electrons can hop. This result can be confirmed by the taken SEM images from the samples with different electrical properties.

In Fig. 2a and b, SEM images of the samples for x = 0.4 ($Er_{0.4}Fe_{0.6}BO_3$) (lowest resistivity) and x = 0.6 ($Er_{0.6}Fe_{0.4}BO_3$) (highest resistivity) are given in order to show the texture relations with the estimated electrical resistivity. Larger grain sizes and higher porosity of the sample $Er_{0.4}Fe_{0.6}BO_3$ than the sample $Er_{0.6}Fe_{0.4}BO_3$ can clearly seen from the figure. Estimated grain sizes for the sample $Er_{0.4}Fe_{0.6}BO_3$ vary from 200 nm to 600 nm (mainly around 450 nm). However, for the sample $Er_{0.6}Fe_{0.4}BO_3$ grain sizes vary from 50 nm to 200 nm; i.e, formed in smaller grains. The porosity in the small particle structure adversely affects the contact of the particles, i.e., for small grain size the contact between the grains may be broken while in the case of large granular structures,

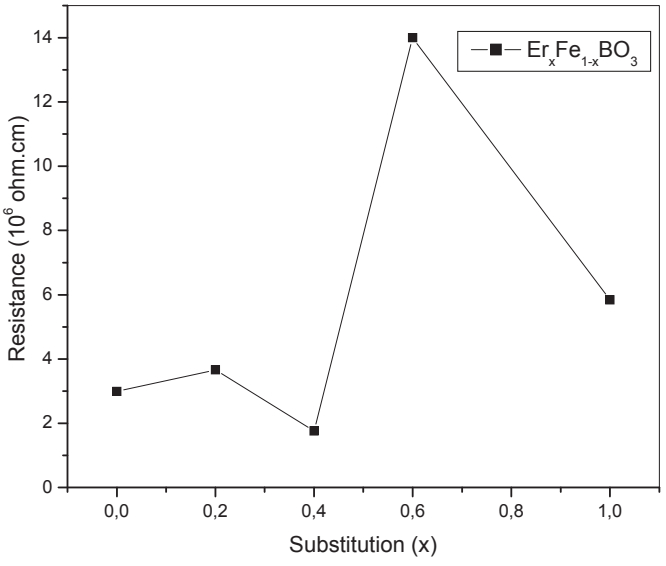


**Fig. 1.** The estimated resistivity values of the $Er_xFe_{1-x}BO_3$ samples.

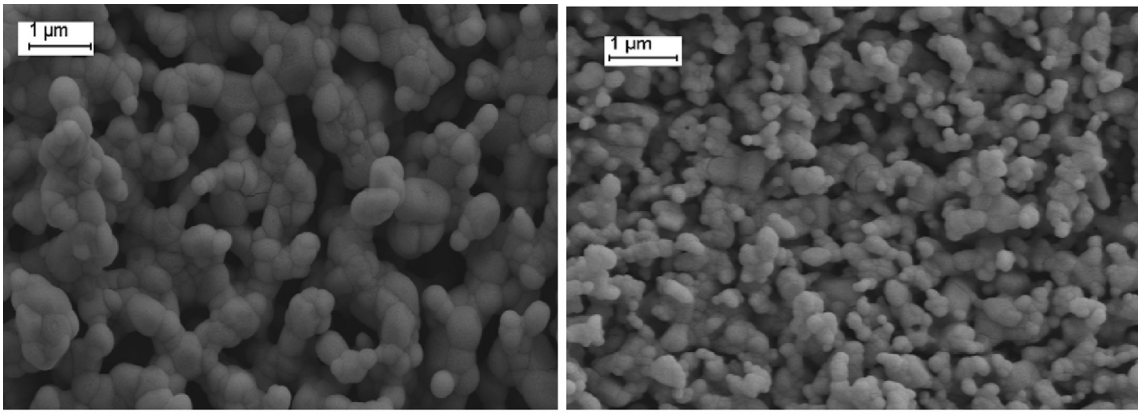


**Fig. 2.** a) SEM image of the sample for x = 0.4 b) SEM image of the sample for x = 0.6.

the structures can remain in contact until further distances. Additionally, during the annealing process up to high temperatures, the constructed crystal structure could be the result of oxygen deficiency that broke down the links with metal atoms. Thus, SEM images presented us a confirmation of the relation between the grain sizes and the electrical conductivity as reported elsewhere [22].

The background information for the crystal structure properties of the samples were studied by the taken XRD patterns. In Fig. 3, XRD patterns of the samples are given in comparison. The crystal structure analysis were carried by MAUD software and the results of the analysis are given in Table 1. According to the figure, the smoothest pattern was taken for the end product $ErBO_3$, and emphasized a more uniform crystal structure in the bulk. However, other end product $FeBO_3$, the XRD pattern has noisy and multiple reflection peaks that points out the polycrystalline nature of the substituted samples with possible defects. The reason for the polycrystalline structures of the samples is the larger atomic volume of the erbium atom that make it not to sit in the iron coordinations but built seperate crystals with different structures than iron centered structures.

The noisy and multiple peak feature of the XRD pattern for the

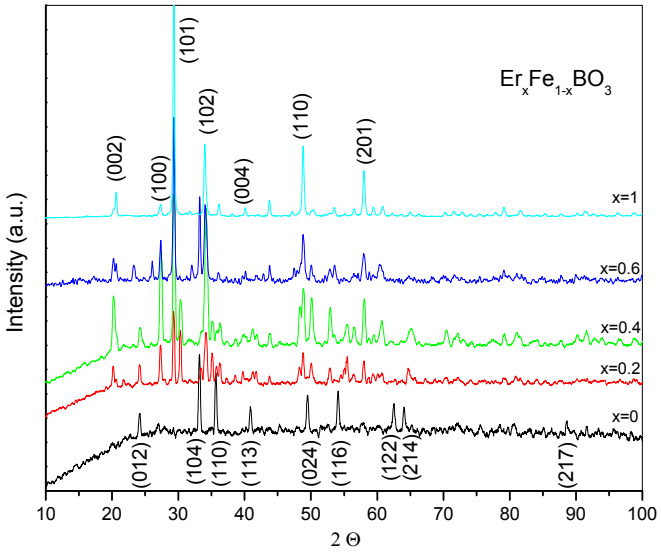


**Fig. 3.** Compared XRD patterns of the samples.

sample x = 0.0 (i.e. $FeBO_3$) emphasizes a polycrystalline structure with a dominant $FeBO_3$ crystal structure and possible defects in the bulk. According to the performed crystal structure analysis, the sample were determined in trigonal (rhombohedral) (78%) $FeBO_3$ crystal geometry with the symmetry space group of "*R "3 c: H*". The determined lattice parameters for the structure in the sample are; a = 5.336 Å and c = 26.267 Å as given in Table 1. Rest (22%) of the sample were determined in hematite ($\alpha$-$Fe_2O_3$) crystal structure (remained parent oxide) with the space group of "*R -3 c: R*". This could happen during the annealing process and points out melted $B_2O_3$ complexes (around 773 K (500 °C)). The lattice parameters of the hematite structures were determined as; a = 5.415 Å and c: 55.723 Å. The base $FeBO_3$ sample was reported as an "insulator" in previous studies [23], however, boron deficiency and polycrystalline feature of the sample seem to cause higher conductivity in the limit of semiconductors ($3.0 \times 10^6$ (ohm.cm)).

According to MAUD analysis, the sample for x = 0.2 (i.e., $Er_{0.2}Fe_{0.8}BO_3$) was determined in two different crystal structure with approximate ratios; 51% of the bulk determined in "$ErFeBO_4$ **"** crystal structure with orthorhombic geometry and "*Pnma*" space group, while the rest (49%) was determined in "$Fe_3BO_5$ " crystal structure with **o**rthorhombic geometry and *Pbam* space group.

As it is given in Table 1 and in Fig. 3, the sample for x = 0.4 was also determined in polycrystalline structure with two different crystal structures: $ErFeBO_4$ structure (like in the sample x = 0.2 but with a higher ratio) (71%) and $Er_3B_5O_{12}$ structure (29%). The structure $Er_3B_5O_{12}$ has orthorhombic geometry with the space group "*Pmna*". Due to rich boron content in the $Er_3B_5O_{12}$ structure, influence of boron atoms on metals (Fe, Er) in the $ErFeBO_4$ structure let Er-Fe blocks interact strongly, built larger molecular bands of Er-B-O via 4*f*-5*d* mixed hybrid band and enrich the quantum symmetries in the compound. Due to quantum selection rules, main problem in such a material is to build up bonds between 2*p* electrons of B, O and 4*f* electrons of Er. As a result of strong interplay between neighboring atoms of 3*d* metal iron, broader molecular bands formed with richer quantum symmetries.

The sample for x = 0.6 was determined with a huge increase in the resistivity (Fig. 1) and noisy XRD pattern (Fig. 3) that highlights the polycrystalline structure with a crystal geometry formation in lower symmetry. According to the MAUD analysis, the sample was dominantly determined (96%) in orthorhombic $ErFeBO_4$ structure as in the samples for x = 0.2 and 0.4. Rest of the sample were determined in monoclinic "$Er_2FeB_4O_{10}$" crystal geometry (with "*P21/c:b1*" space group) with a small ratio (4%) in the bulk which can be treated as a volumetric defect. The disturbance in the bulk is

**Table 1**
Crystal structure analysis of the $Er_xFe_{1-x}BO_3$ samples.

| Substitution ($Er_xFe_{1-x}BO_3$) | Crystal | α | β | γ | a | b | c | Geometry | SG | % |
|---|---|---|---|---|---|---|---|---|---|---|
| X = 0 | $FeBO_3$ | 90 | 90 | 120 | 5.366 | 5.366 | 26.267 | Trigonal | R-3c:H | 78 |
| | $Fe_2O_3$ | 90 | 90 | 120 | 5.415 | 5.415 | 55.723 | Trigonal | R-3c:R | 22 |
| X = 0.2 | $Fe_3BO_5$ | 90 | 90 | 90 | 9.318 | 12.226 | 3.072 | Orthorhombic | Pbam | 49 |
| | $ErFeBO_4$ | 90 | 90 | 90 | 9.832 | 4.464 | 8.802 | Orthorhombic | Pnma | 51 |
| X = 0.4 | $ErFeBO_4$ | 90 | 90 | 90 | 17.696 | 6.674 | 3.201 | Orthorhombic | Pnma | 71 |
| | $Er_3B_5O_{12}$ | 90 | 90 | 90 | 12.677 | 4.774 | 12.149 | Orthorhombic | Pmna | 29 |
| X = 0.6 | $ErFeBO_4$ | 90 | 90 | 90 | 9.277 | 3.176 | 9.629 | Orthorhombic | Pnma | 96 |
| | $Er_2FeB_4O_{10}$ | 90 | 90.01 | 90 | 4.531 | 7.219 | 9.295 | Monoclinic | P21/c:b1 | 4 |
| X = 1.0 | ErBO3 | 90 | 90 | 120 | 3.744 | 3.744 | 8.771 | Hexagonal | P-62c | 100 |

probably responsible for the decrease in the electrical conductivity. This crystal structure was presented in the crystallography database as "$Er_2CuB_4O_{10}$" structure and, in this study, Fe atoms sit in the Cu coordinations [24].

The sample for x = 1.0 is $ErBO_3$ and it was the second end product sample. $ErBO_3$ has also studied many times in the literature [25,26]. Low noise in the XRD pattern of the sample confirms one crystal structure formation in the sample. According to the XRD pattern analysis, crystal geometry of the $ErBO_3$ sample was determined in hexagonal geometry with a space group of "P63/mmc" (100%). Detailed crystal structurel information about $ErBO_3$ is given in Table 1. Hexagonal geometry of the sample provided better conductivity than the sample for x = 0.6, but worse than other samples; the orthorhombic (x = 0.2 and 0.4) and trigonal $FeBO_3$. This can be due to the constructed isolated molecular islands around the heavy fermion Er. Like the iron atoms in $FeBO_3$ structure, erbium atoms link to the $BO_3$ ligands via oxygen atoms. The reason of the higher resistance in the sample can be the contribution of the heavy Er atoms to the interstitial potential. Higher potential of erbium add an extra resistance to electrons' motion by increasing the potential between atomic distances where electrons travel. XAFS study can provide us precious data both the on crystal structure and electronic interactions between the neighboring atoms.

In Fig. 4, XAFS spectra for the sample x = 0.0 ($FeBO_3$) is given for Fe K-edge. XAFS measurements with higher energy absorption process than the bonding energy of electrons are called as XAFS (x-ray absorbing thin-film spectroscopy) and can be divided into two parts: XANES and EXAFS (shown by dashed lines in the figure). XANES region can provide fruitful information about the electronic structure, bonding and chemical environment etc. The region may also contain a "pre-edge" part just placed below the main absorption edge and highlights the forbidden transitions, crystal disorders, asymmetries in the structure. The pre-edge part in Fig. 1 is circled with a dashed line on the spectra.

Fe K-edge XAFS spectra of the $FeBO_3$ sample begin to rise at 7104 eV and give a maximum at 7132 eV. Main peak is due to the 1*s* electrons' transition to the unoccupied 4*p* levels. Actually, unoccupied 3*d* levels should be the final state for 1*s* electrons during the excitation process, but due to quantum selection rules $1s \rightarrow 3d$ transition is forbidden. However, if the outer shell electrons of the neighbors overlap with each other and cause a coupling or hybridization, molecular band built with the 3*d* levels can gain additional *p* or *f* symmetries. Presence of *p*-symmetry in the lower energy levels make the *s* electrons' transition to the hybridized 3*d* levels possible. When such an excitation occurs, the absorption spectra give a peak at the pre-edge region as an indicator of the avoided forbidden transitions, like the tiny pre-edge feature at 7114 eV. Low absorption intensity of the pre-edge structure confirms the weak hybridization between 2*p* levels of O, B and 3*d* level of Fe. Beyond the pre-edge peak, the main absorption edge begins. The intensity of the main absorption edge spectra is related with the unoccupied states at the valence level. The sharp peak and higher intensity of the K-edge confirms the mixing between valence *3d-4p* levels of Fe atom; i.e. $3d^5 4p^1$. The main absorption peak is a result of 1*s* electrons transition to 4*p* levels of iron. The main edge spectra with a small edge feature beyond the maximum is a result of the occured different site symmetry in the sample, i.e., $\alpha$-$Fe_2O_3$. The first peak at 7133.74 eV correspond to the absorption intensities from the $Fe^{3+}$ ions in the $FeBO_3$ sites, while the second peak at 7145.9 eV correspond to the absorption from the $Fe^{3+}$ ions in the $\alpha$-$Fe_2O_3$ sites.

Beyond the absorption edges of the Fe K-edge spectra, extended-XAFS part (EXAFS) lies as a result of photoelectrons' scattering processes. This part can be processed to yield data on the atomic coordinations and distances from the source atom of the photoelectron. EXAFS technique provides useful tools for better analysis by deriving information from the periodicity of the oscillations in the EXAFS region. By the extracted EXAFS data, one can estimate the bond lengths, the amplitudes of the fine structure and the number of atoms with corresponding wave numbers (*k*). EXAFS scattering intensities of the samples are given in comparison in Fig. 5. The sample for x = 0.0 has the smoothest scattering data among the samples. The smooth shape points out higher

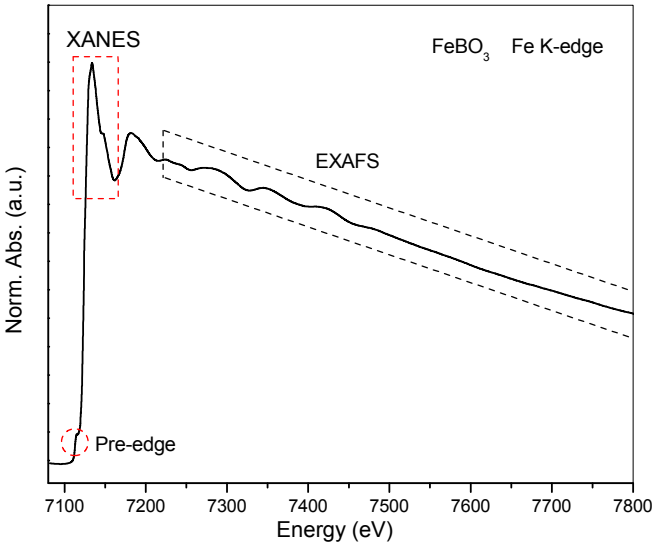


**Fig. 4.** Fe K-edge XAFS spectra of $FeBO_3$.

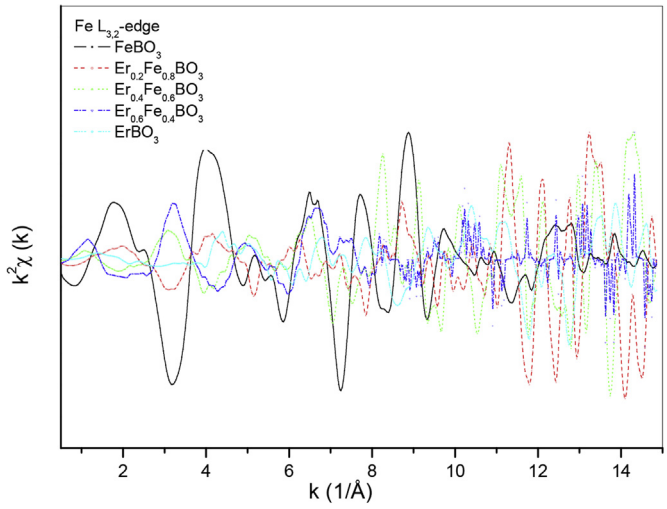


**Fig. 5.** Comparison of the EXAFS "chi" (χ) scattering intensities of the studied samples.

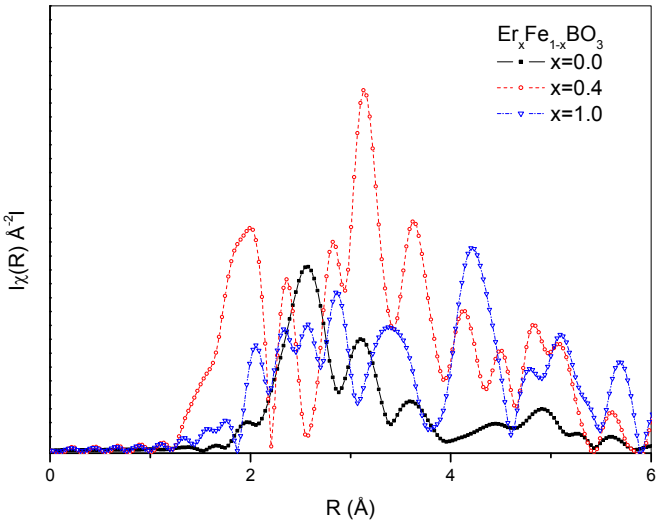


**Fig. 6.** Radial Distribution Function (RDF) of the samples for x = 0.0, 0.4 and 1.0.

uniformity and homogeneity in atomic and interstitial potential in the sample than others. Er substituted samples, mainly, showed noisy and corrupted-like scattering data confirming the polymorphism in the bulk containing light and heavy atoms together. However, the scattering data of the sample for x = 1.0 has a rough data with lowest intensity among samples. Heavy fermion "erbium" atom provides high potential values to the interstitial media in the bulk where photoelectrons travel and high interstial potential reduced the kinetic energy of the photoelectron. However, the stability in the scattering intensity along the *k*-values is a result of one type of crystal structure in the sample bulk. The initial sample (x = 0.0) has higher intensities at lower *k*-values and a decay at high *k*-values that points out longer mean free path among others for the photoelectrons in the sample ($k \sim 1/\lambda$). However, substituted samples have high scattering intensities at high *k*-values (short mean free path). Both the presence of heavy atom erbium with light atoms (O, B, and Fe) and the heterogeneity in interstitial potential due to polycrystalline feature of the samples are the reason of the noisy and high *k*-valued scattering intensity of the substituted samples. The overlap between the outer shell electrons of the metal atoms (Er and Fe) and the light O atoms cause potentially high energy regions in the interstitial regions between highly densed atomic environment. During the travel of the photoelectrons, these kind of regions behave like electron traps and cause a decay in photoelectrons' kinetic energies.

The fourier transform of the EXAFS "chi" (χ) scattering intensity yield the "Radial Distribution Function" (RDF) and provides the atomic distances to the source atom. The RDF data analysis of the samples were derived as a combination of collected EXAFS data and XRD pattern analysis. To determine the exact atomic locations and types, EXAFS calculations were performed with the scientific code FEFF 8.2. The input files for the calculations were prepared with the obtained analysis results of the XRD patterns via MAUD analysis. Fitting processes results for the samples are given in Table 1. The comparison of the end product samples are given with the substituted sample x = 0.4 in Fig. 6; i.e., x = 0.0 (78% $FeBO_3$+22% $Fe_2O_3$), x = 0.4 (71% $ErFeBO_4$+29% $Er_3B_5O_{12}$) and x = 1.0 ($ErBO_3$). To make the figure more clear and avoid from the complexity, RDF data for the samples x = 0.2 and 0.6 are not given but their analysis results are also given in Table 2.

In the RDF data, an atom (the source atom) sits at the origin and the atomic coordinations around the source atom in the sample are given on a one dimensional axis. The peak intensities are related with the number of the atomic coordinations and the atomic weights. The atomic types from the radial distribution function data are determined by the k-weight study of the scattering intensities in the figure. In general, oxygen and boron atoms are located in the close neighborhood of Fe or Er due to ionic properties and related overlapping occurring between the outer shells' and outer shell electrons' wavefunctions. Wide and gaussian shape of the peaks are due to the overlapped signals of oxygen and boron atoms that located slightly different coordinations or bonded with different angles.

The multiple peak structure of the RDF data is highly related with the polycrystalline structure with different geometry in the samples. Tiny edge-like structures on the large peak intensities emerge as a result of the overlapped signals of the light atoms which are located closer to eachother between heavier atoms (Fe, Er). In both $FeBO_3$ and $ErBO_3$ structures, metal atoms (Fe, Er) bond with the $BO_3$ ligands via oxygen atoms and form different crystals structures but remain incomplex and richer in site symmetry. Due to the higher electronegativity properties of the boron atoms, they can located in closer distances to oxygen atoms and yield narrower peaks with superposed peaks on the RDF data. The closest atomic neighbors in each crystal structures are given in Table 1.

To understand the background mechanism of the overlapped signals and for further analysis (an extra view for the electronic properties), XANES measurements were performed at room temperatures for iron $L_{3,2}$-edges. The Fe $L_{3,2}$-edge spectra are so sensitive to its chemical environment and comparison of spectra of the samples are given in Fig. 7.

The $L_3$-edge spectra appear as a result of $2p_{3/2}$ electrons' transitions to unoccupied 3*d* levels, while the $L_2$-edge spectra are due to transitions to unoccupied levels of $2p_{1/2}$ electrons'. The $L_3$-edge spectra of the samples begin to rise at 705 eV and commonly have two maxima. The spectra for $FeBO_3$ crystal has two peak on the main absorption edge at 706.5 eV and 708 eV, which are attributed to different oxidation states of iron in hematite ($\alpha$-$Fe_2O_3$) and $FeBO_3$, respectively. The sharp intensity of the main edge absorption spectra is related to the unoccupied states at the valence level. The $L_2$-edge absorption spectra also have similar double peak structure like $L_3$-edge. $L_2$-edge spectra begin to rise at 718 eV and have maxima at 719.5 eV and 721 eV, respectively.

The maxima on the Fe $L_3$-edge XANES spectra of the sample for x = 0.2 are at 705 eV and 706.8 eV. The energy shifts to lower energy values of the substituted samples on the Fe $L_3$-edge spectra are result of the richer site symmetries of the Er- substituted

**Table 2**
EXAFS analysis results of the samples for the nearest neighboring atomic types.

| Sample ($Er_xFe_{1-x}BO_3$) | Crystal | Source Atom | Atomic Distances | R (Å) | Degeneracy | $\sigma^2$ (Å$^2$) |
|---|---|---|---|---|---|---|
| X = 0 | $FeBO_3$ | Fe | Fe-O | 2.892 | 6 | 0.03625 |
| | | | Fe-B | 3.793 | 6 | 0.05689 |
| | | | Fe-Fe | 5.363 | 6 | 0.01797 |
| | $Fe_2O_3$ | Fe | Fe-Fe | 3.701 | 3 | 0.01383 |
| | | | Fe-O | 4.088 | 3 | 0.03642 |
| X = 0.2 | $ErFeBO_4$ | Er | Er-O | 1.841 | 2 | 0.01359 |
| | | | Er-Fe | 2.232 | 2 | 0.00648 |
| | | | Er-B | 3.376 | 2 | 0.02715 |
| | | | Er-Er | 3.380 | 2 | 0.00570 |
| | $Fe_3BO_5$ | Fe | Fe-O | 1.869 | 1 | 0.03056 |
| | | | Fe-Fe | 2.731 | 1 | 0.01643 |
| | | | Fe-B | 2.981 | 1 | 0.05649 |
| X = 0.4 | $ErFeBO_4$ | Er | Er-Er | 2.254 | 2 | 0.00455 |
| | | | Er-O | 2.552 | 2 | 0.01708 |
| | | | Er-Fe | 3.201 | 2 | 0.00807 |
| | | | Er-B | 4.320 | 2 | 0.02750 |
| | $Er_3B_5O_{12}$ | Er | Er-O | 2.222 | 2 | 0.01606 |
| | | | Er-B | 3.028 | 2 | 0.02559 |
| | | | Er-Er | 3.377 | 1 | 0.00279 |
| X = 0.6 | $ErFeBO_4$ | Er | Er-Fe | 1.588 | 2 | 0.00494 |
| | | | Er-O | 1.690 | 2 | 0.01388 |
| | | | Er-B | 3.368 | 2 | 0.02741 |
| | | | Er-Er | 3.567 | 2 | 0.00578 |
| | $Er_2FeB_4O_{10}$ | Er | Er-Fe | 3.195 | 1 | 0.00572 |
| | | | Er-O | 2.199 | 1 | 0.01603 |
| | | | Er-B | 3.032 | 1 | 0.02561 |
| | | | Er-Er | 3.424 | 1 | 0.00280 |
| X = 1.0 | ErBO3 | Er | Er-O | 1.556 | 6 | 0.01517 |
| | | | Er-Er | 2.162 | 6 | 0.00264 |
| | | | Er-B | 2.457 | 6 | 0.02563 |

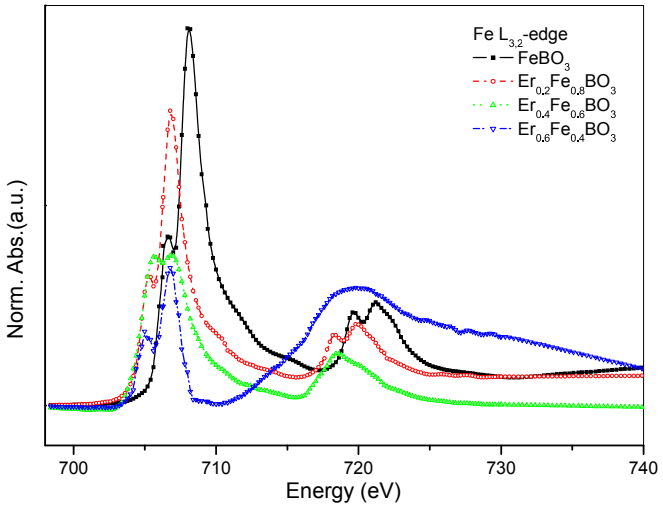


**Fig. 7.** Fe $L_{3,2}$-edge XANES spectra of $FeBO_3$ sample.

sample provided by the neighboring atoms in the samples. The shift emphasizes broader molecular bands built by the stronger overlap between Fe outer shell electron wavefunctions with its neighboring atoms' outer shell electrons. In other words, the strong overlap is a result of rare-earth erbium presence in the sample with its 4*f* electrons. The overlap built between Er 4*f* and Fe 3*d*-*O2p* hybridized levels and give the highest peak at 706.8 eV due to increased number of unoccupied states.

The Fe $L_{3,2}$-edge spectra of the sample for x = 0.4 gave two maxima at 705.7 eV and 706.9 eV as a result of spin-orbit coupling, respectively. The sample (x = 0.4) was determined in two different crystal structure, but only one crystal structure was containin iron in its crystal structure; $ErFeBO_4$. Despite the polycrystalline structure of the sample, no pre-edge was appeared on the spectra and highlights symmetry in the close environment of the Fe atoms occured. The smooth character of the $L_3$-edge below the main-edges, points out the strongly overlapped outer shell electrons in the neighborhood. The strong overlap between heavy fermion Er and Fe atoms constructed larger molecular bands and cause a splitting in the energy levels because of the interaction between electron spin and its orbits magnetic moments. The “one” peak feature on the $L_2$-edge confirms the single crystal structure with iron atoms in the sample and the coupling showed itself with a weak splitting.

The Fe $L_{3,2}$-edge spectra of the sample x = 0.6 also have two peak structure, like the samples x = 0.0 and 0.2, and emphasize different site symmetries of iron atoms in the sample, i.e., $Er_2FeB_4O_{10}$ and $ErFeBO_4$. The spectra has a tiny pre-edge feature at 703 eV as result of the low site symmetry in the bulk indicating the 3*d*-4*f* hybdridization. The lower peak energy on the main edge was determined at 705.5 eV and the highest peak energy were determined at 707 eV. Similar multiplet structure also observed on the large and noisy $L_2$ edge spectra which points out the corruptive feature of the new geometry that may behave like a defect in the bulk.

To observe the f-electrons' activity in the bonding interactions with oxygen and boron, XANES study of the end product sample $ErBO_3$ (without the presence of iron) is a good choice. The $L_3$-edge of the erbium atoms was selected to collect the absorption data at BL8 of SLRI and given in Fig. 8. Smooth Er $L_3$-edge absorption

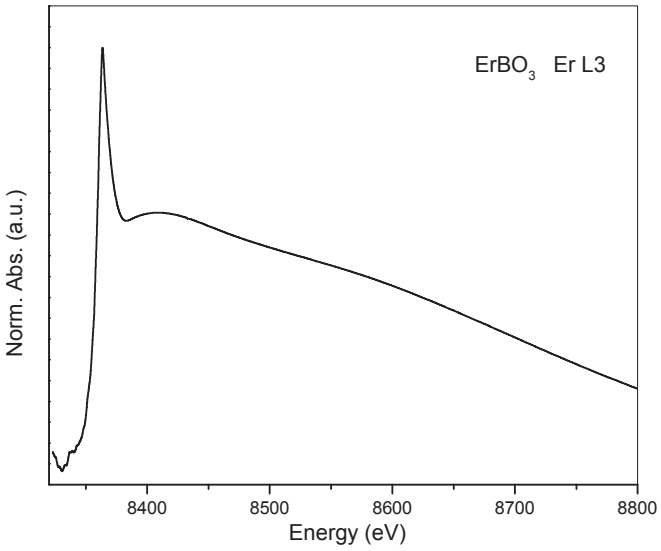


**Fig. 8.** XANES spectra of the Er $L_3$-edge in the sample $ErBO_3$.

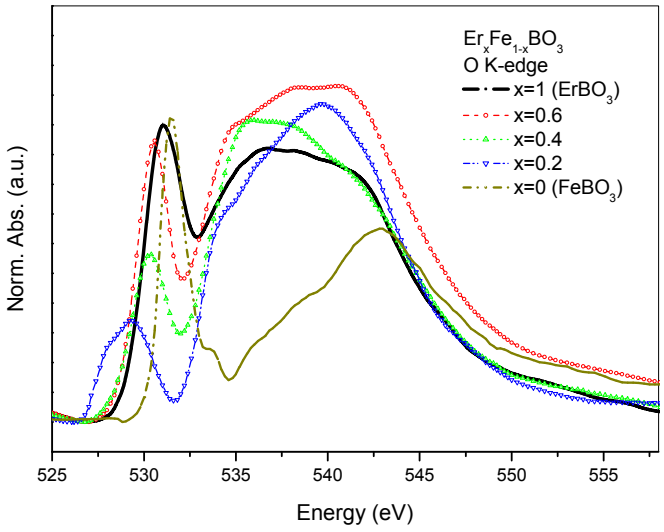


**Fig. 9.** Compared Oxygen K-edge spectra of the samples $Er_xFe_{1-x}BO_3$.

spectral structure confirms the higher symmetry in the crystal geometry. In case of transitions of excited electrons to the *f*-level of Er, a pre-edge feature should appear below the main edge on the spectra due to the dipole selection rules (forbidden transition; p→f). The $L_3$-spectra begin to rise at 8329.6 eV and have a maximum at 8363 eV. A weak shoulder like pre-edge at 8336.6 eV appeared on the $L_3$-edge spectra as a sign of weak *4f* level contribution to the molecular band. Outer shells of the neighboring atoms O and B are the *p*-levels which can not also contribute to *f*-levels of the Er atoms due to forbidden transition. So it is clear that, only 5*d* levels of erbium are available for excited 2*p* electrons to make free transitions as a final state or 2*p* electrons of oxygen to interact for bonding. Weak pre-edge feature on the pre-edge is a sign of low amount of the excited 2*p* electrons make transitions to the mixed 4*f* 5*d* levels of Er. In fact, it was expected that the pre edge region would give a more severe peak, but the presence *dp*-symmetry due to Er-O interplay, the dipole selection rules weakens the transitions.

Oxygen is the common atom in the samples and link all atoms with eachother to build molecules. So, oxygen is a good choice to study the electronic interplay comparison for the samples. In Fig. 9, normalized O K-edge spectra of all studied samples are given in comparison. In the figure, all measured spectra are normalized to study on the spectral features better. However, the raw data of the O K-edge absorption spectra can give an estimation of the oxygen stoichiometries in the sample for comparison. For this aim, spectral areas of the O K-edge raw spectra were calculated and normalized to the value of the base oxide $FeBO_3$. According to the calculations, the results of the areal ratios are; 0.0494 (x = 1.0), 1.71 (x = 0.6), 0.981 (x = 0.4), 0.910 (x = 0.2) and 1.0 (x = 0.0), respectively. The results points out a relation between the resistivity and oxygen stoichiometry in the samples.

The K-edge absorption spectra is due to *1s* core electrons' transition to the unoccupied *2p* valence levels as a final state. The spectra in the figure begin to rise at 528 eV (except for the sample x = 0.2) and all have a sharp pre-edge structure. The intensity of the pre-edge structure is related with the number of unoccupied states on the hybridized levels and also the strength of the overlapped hybridized levels. The pre-edge structure of the sample $FeBO_3$ has a maximum at 531.5 eV while $ErBO_3$ has maximum at 531 eV. The 0.5 eV energy shift to lower energy side in $ErBO_3$ highlights the electron gain of the O atoms during bond formation with overlapped outer shell electrons. The decrease on the pre-edge structure intensity in Er doped samples highlight the weaker hybridized bonds built between heavy and light atoms; i.e. *f*-level. This is also confirmed by the larger main absorption edges of the samples than $FeBO_3$ sample. Especially, the splitted pre-edge peak on $ErBO_3$ sample with higher intensity points out the hybridization between Er 5*d* and O 2*p* levels. Similar pre-edge feature also presented in the sample for x = 0.2. The pre-edge peak has lower intensity but the broader energy range emphasized wide molecular band with low energy levels due to *f-d* symmetry rich hybridization.

## 4. Conclusions

In this study, materials with the general formula $Er_xFe_{1-x}BO_3$ were investigated upon their crystal, electrical and electronic structure properties. New crystal geometries for Er-Fe complexes were determined with the varying "x" concentrations. Besides, Er substitution and boron decificiency (in the samples) were determined to cause corruptive domains that weaken the bonds or ruins the symmetry in the bulk. Among the substituted samples, sample for x = 0.4 was determined the most interesting sample showing better conductivity with strongest overlapped electronic levels that built larger molecular bands. Larger grain sizes and strong overlapped hybridized molecular bands built between heavier Er and Fe atoms were determined as the main reasons emerging such properties of the sample x = 0.4 via 3*d*-4*f* interplay. Besides, the relation between grain size and resistivity was also confirmed.

## Acknowledgements

The author would like to thank to Dr. Gunnar Ohrwall from MAX-lab. Beamline I1011 (Lund, Sweden), to Dr. Wantana Klyusubun and her staff from SLRI (Siam Photon) both for their technical support and great hospitality. This study is supported financially by "BAP-TTEF EEEME (OMÖ) 2012-7" project of Mersin University (Mersin, Turkiye). Additionally, the research leading to these results has received funding from the European Community's Seventh Framework Program (FP7/2007-2013) CALIPSO under grant agreement no 312284.

## References


[1] C. Ruihua, C.N. Borca, P.A. Dowbena, S. Stadler, Y.U. Idzerda, Appl. Phys. Lett. 78 (4) (2001) 521.
[2] H.S. Nabi, R. Pentcheva, Phys. Rev. B 83 (2011) 214424.
[3] E.A. Moore, Phys. Rev. B 76 (2007) 195107.
[4] Y.W. Liu, X.F. Rui, Y.Y. Fu, Y.W. Han Zhang, J. Metastable Nanocrystalline Mater. 23 (2005) 243.
[5] I. Bernal, C.W. Struck, J.G. White, Acta Crsytallogr. 16 (1963) 849.
[6] H. Schmid, Acta Crsytallogr. 17 (1964) 1080.
[7] J.C. Joubert, T. Shirk, W.B. White, R. Roy, Mater. Res. Bull. 3 (1968) 671.
[8] N.V. Kazak, A.M. Potselvyko, S.G. Ovchinnikov, A.S. Alexandrovski, V.A. Chernov, V.V. Rudenko, Phys. B 378–380 (2006) 327–329.
[9] R. Diehl, Solid State Commun. 17 (1975) 743–745.
[10] P. Becker, Adv. Mater. 10 (1998) 979–992.
[11] V.N. Zabluda, S.G. Ovchinnikov, A.M. Potseluiko, S.A. Kharlamova, Phys. Solid State 47–3 (2005) 489–494.
[12] M.W. Lufoso, P.M. Woodward, Acta Cryst. B 57 (2001) 725–738.
[13] R.L. White, J. App. Phys. 40 (1969) 1061–1069.
[14] M. Marezio, J.P. Remeika, P.D. Dernier, Acta Cryst. B26 (2008) 2022.
[15] L. Lutterotti, D. Chateigner, S. Ferrari, J. Ricote, Thin Solid Films 450 (2004) 34–41.
[16] I.A. Kowalik, G. Öhrwall, B.N. Jensen, R. Sankari, E. Wallen, U. Johansson, O. Karis, D. Arvanitis, J. Of Phys. Conf. Ser. 211 (2010) 012030.
[17] A.L. Ankudinov, B. Ravel, J.J. Rehr, S.D. Conradson, Phys. Rev. B 56 (1997) R1712.
[18] B. Ravel, J. Synchrotron Radiat. 8 (2) (2001) 314.
[19] B. Ravel, M. Newville, J. Synchrotron Radiat. 12 (4) (2005) 537.
[20] W. Klysubun, et al., Commission and performance of x-ray absorption beamline at the Siam photon laboratory, Nucl. Instrum. Methods Phys. Res. A 582 (2007), 87W.
[21] Klysubun et al., X-ray absorption spectroscopy beamline at the Siam Photon Laboratory, AIP Conference Proceedings 2006;879:860.
[22] A. Tschöpe, Solid State Ionics 139 (3–4) (2001) 267–280.
[23] R. Wolfe, A.J. Kurtzig, R.C. LeCraw, J. Appl. Phys. 41 (1970) 1218.
[24] J. Schaefer, K. Bluhm, Z. fuer Naturforsch. Teil B. Anorg. Chem. Org. Chem. (42, 1987-) 50 (1995) 1141–1145.
[25] M. Eibschuts, L. Pfeiffer, J.W. Nielsen, J. Appl. Phys. 41 (1970) 1276.
[26] A. Pitscheider, K. Reinhard, O. Oeckler, H. Huppertz, J. Solid State Chem. 184–1 (2011) 149–153.